Nonequilibrium effects in the $^{139}La+^{40}Ar$ reaction at 10 MeV per nucleon observed in a study of neutron emission

J. L. Wile, S. S. Datta, W. U. Schröder, J. R. Huizenga,
J. Tôke, and R. T. de Souza*
Departments of Chemistry and Physics and Nuclear Structure Research Laboratory, University of Rochester, Rochester, New York 14627
(Received 27 December 1988)

Energy spectra of neutrons emitted in the damped reaction $^{139}La+^{40}Ar$ at $E_{lab}=400$ MeV were measured at eight angles in coincidence with projectile-like reaction fragments, using a time-of-flight technique. Apart from a small high-energy component, the angular and energy distributions of neutrons were found to be well described by assuming two sources moving at the velocities of the light and heavy reaction fragments emitting isotropically in their rest frames. The logarithmic slopes of the neutron energy spectra and the corresponding multiplicities of neutrons from the two sources suggest that the projectile-like fragment receives more than its equilibrium share of excitation energy for all values of total kinetic energy loss. Detailed statistical calculations indicate that the amount of excitation energy generated in each fragment is well described by the one-body nucleon exchange model. The high-energy component in the neutron energy spectra has properties that are consistent with preequilibrium neutron emission. Averaged over all energy losses greater than 20 MeV, this "preequilibrium" neutron multiplicity is approximately equal to 0.1. However, the intensity of this component increases as the impact parameter decreases.

I. INTRODUCTION

Light-particle emission from highly excited primary reaction products provides an effective tool for investigating the properties of heavy-ion reaction mechanisms. Such studies[1] have demonstrated the relatively gentle nature of heavy-ion collisions at bombarding energies of a few MeV per nucleon above the Coulomb barrier. Results of earlier measurements[2–4] of neutron evaporation spectra from damped reactions were interpreted in terms of an intermediate dinuclear system that achieves thermal equilibrium during a collision. In these experiments, the measured spectrum of neutrons emitted by the projectile-like reaction fragment had essentially the same slope as the energy spectrum of neutrons from the target-like fragment. Assuming that the observed logarithmic slopes of the neutron energy spectra directly reflects the temperature of the emitting primary nucleus, these works concluded that even in fast, partially damped collisions, the dinuclear system achieved thermal equilibrium. It has subsequently been demonstrated,[5] however, that the relationship between the slopes of the emitted particle energy spectra and the temperatures of the primary emitting nuclei can be established only via complex simulation calculations. A reinterpretation[5,6] of the neutron energy spectra and neutron multiplicity data[2] from the $^{165}Ho+^{56}Fe$ damped reaction showed that the excitation energy ratio (E_{PLF}/E_{TLF}) of the primary projectile-like fragments (PLF) and target-like fragments (TLF) was larger than predicted[1] for thermal equilibrium, although the magnitude of the disparity decreased with increasing energy loss. Hence the lifetimes of the intermediate dinuclear complex in damped nuclear reactions of asymmetric systems are, in general, too short to attain thermal equilibrium between projectile-like and target-like fragments.

Over the last five years, considerable independent evidence[1,7–14] has been reported to support the conclusion that the dinuclear complex does not attain thermal equilibrium in damped nuclear collisions. One novel study[8] measured the peak-to-valley ratio of the bimodal mass distributions from sequential fission of the uranium-like fragment in partially damped $^{238}U+^{56}Fe$ collisions. At low kinetic energy losses, it was found that the heavy, uranium-like fragment received less excitation energy than predicted for a thermally equilibrated dinuclear system, implying that the light, iron-like fragment receives energy in excess of the equilibrium amount. In contrast to the above results, radiochemical[15,16] studies of the partition of excitation energy, assuming instantaneous A/Z equilibration, conclude that for reactions with long interaction times and significant net mass transfer to the light fragment, cold heavy fragments are produced. Independent measurements[9–11] of quasielastic reactions also indicate that the dissipated energy deposited in a reaction fragment is correlated with the net mass transfer.

Measurements of sequential particle evaporation, however, provide the most general method of determining the excitation energy partition in damped reactions. After separation of the dinuclear system, the bulk of the excitation energy is carried away by neutrons evaporated from the two fully accelerated primary fragments. Particle evaporation measurements are usually not limited by intrinsic constraints that allow only a small range in energy loss, unlike some of the methods discussed above, and the calculations required to interpret the data are straightforward and well understood.[1] In particular, exclusive neu-

tron emission experiments for heavy systems provide a relatively simple means of tracking energy relaxation from partially damped collisions to the most strongly damped collisions. However, detailed studies of this kind are extremely rare. Additional exclusive neutron experiments combined with realistic simulation calculations, then, are of high current interest for the further development of a quantitative theory of damped reactions.

One theory that has met with considerable success at describing data acquired for heavy-ion collisions induced at bombarding energies of a few MeV per nucleon above the Coulomb energy at the interaction radius is the one-body nucleon exchange transport model (NEM). In this approach,[17,18] all dinuclear relaxation mechanisms are mediated by the exchange of independent nucleons between the reaction partners. In the model, the excitation energy generated in the recipient nucleus by a transferred nucleon is mainly determined by the velocity mismatch between the interacting nuclei. Hence, on the average, each nucleus receives a comparable amount of excitation energy. The temperature gradient generated by this process in an asymmetric reaction tends to drive the system from equipartition to an equilibrium sharing of the total available excitation energy between the reaction partners. This equilibrium limit can only be reached for significantly long interaction times. Several of the experimental observations[5–8,12–14] discussed above are, in general, consistent with the predictions of the NEM approach while others[9–11,14–16] appear to be at variance with this model.

The present work represents the first in a series of experiments with the heavy system ^{40}Ar+^{139}La. The choice of this system represents a compromise between a large initial mass asymmetry, which should enhance nonequilibrium excitation energy sharing, and a minimum chance of projectile breakup or sequential fission of the target-like fragment. The bombarding energy of 10 MeV per nucleon, corresponding to 6.2 MeV per nucleon above the Coulomb barrier, was chosen in an attempt to observe the onset[1] of preequilibrium neutron emission in this reaction. Table I lists relevant parameters for the ^{139}La+^{40}Ar reaction at $E_{lab}=10$ MeV per nucleon.

A discussion of the exprimental procedure will be given in Sec. II, followed by a description of the data analysis in Sec. III. Results of the measurement and their interpretation will be presented in Sec. IV, followed by a summary of the conclusions of this work in Sec. V.

TABLE I. Characteristic reaction parameters for the system ^{139}La+^{40}Ar at $E_{lab}=10.0$ MeV per nucleon.

Composite system:	^{179}Re
Reduced mass	$\mu=31.1$ u
Strong-absorption radius	$R_{SA}=12.5$ fm
Coulomb barrier	$V_c(R_{SA})=118.5$ MeV
Energy above Coulomb barrier	$(E_{c.m.}-V_c)/\mu=6.2$ MeV per nucleon
Laboratory grazing angle	$\theta_{1/4}=21.3°$
Grazing angular momentum	$l_{max}=210\hbar$
Total reaction cross section	$\sigma_R=3.0$ b
Maximum angular momentum for fusion	$l_{crit}=109\hbar$
Fusion cross section	$\sigma_{fus}=0.8$ b
Liquid drop limit of stability	$l_{RLDM}=82\hbar$

II. EXPERIMENTAL PROCEDURE

The aim of the present experiment was to measure neutron energy spectra in coincidence with projectile-like reaction fragments. A schematic diagram of the experimental setup is given in Fig. 1. A 500-μg/cm^2-thick ^{139}La target was located in a 25.4-cm-diam aluminum scattering chamber with a 5-mm-thick wall. The target was bombarded with 400-MeV ^{40}Ar projectiles accelerated by Lawrence Berkeley Laboratory's 88-inch cyclotron. The beam dump was heavily shielded with concrete, paraffin, and organic liquid, in order to reduce the background neutrons produced by the beam in the Faraday cup. One solid-state detector (SSD) telescope was placed at a laboratory angle $\theta_{HI}=-20°$ in the plane of the neutron detectors surrounding the chamber, while another was placed at a position defined by an in-plane angle of 35° and an out-of-plane angle of 40°. Both detectors were approximately 7 cm away from the target. These detector telescopes were comprised of 50-μm-thick transmission detectors and 100-μm-thick stop detectors, and were used to detect projectile-like fragments from the damped reaction. Eight neutron detectors were placed approximately 1 m away from the target and at various angles θ_n about the target chamber. The neutron detectors consisted of 12.7-cm diam by either 3.8- or 5.1-cm-thick NE213 liquid scintillators backed by Amperex XP2041 photomultipliers. As illustrated in Fig. 1, four thin plastic scintillator detectors ("proton paddles") were placed at forward angles in order to detect high-energy protons that were capable of escaping the target chamber. Any neutron detector signal in coincidence with a signal from the proton paddles was assumed to be caused by a proton

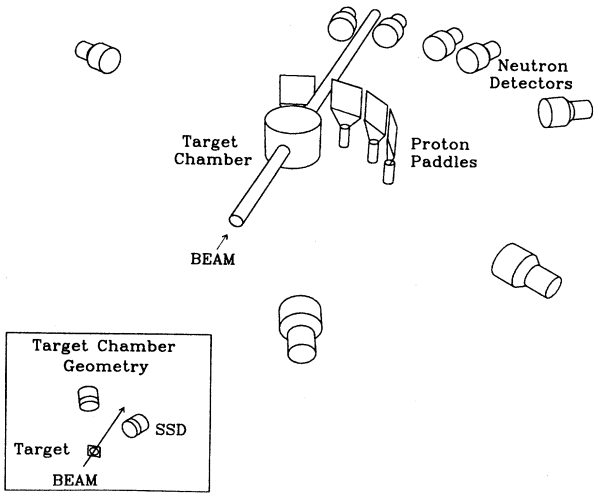

FIG. 1. Schematic diagram of the experimental setup.

and was vetoed in the final analysis.

The heavy-ion telescopes provided start signals, while the neutron detectors provided the stop signals for the neutron time-of-flight (TOF) measurement. The time between these two signals, differing from the true neutron TOF by the TOF of the heavy-ion, was measured using a time-to-digital converter (TDC). Pulse-shape discriminators developed at the Hahn-Meitner-Institut in Berlin provided efficient neutron-γ selection, and the time resolution was 0.75 ns for γ rays in coincidence with quasielastic events. The scintillator light output was also measured with the neutron detectors, and a discriminator level of approximately 0.5 MeV was set on this light output spectrum. An event was recorded if one of the heavy-ion telescopes and at least one of the eight neutron detectors had fired. In addition, for every 1000 events that were detected by each heavy-ion telescope, one event was collected regardless of whether or not the neutron detectors had fired, in order to accumulate a singles heavy-ion spectrum for normalization purposes.

Figure 2 shows a typical TOF spectrum for events identified as neutrons by a pulse-shape discriminator. The narrow spike to the left of the broad neutron peak is caused by the few γ rays (1:1500) allowed to be accepted by the pulse-shape discriminator. Favorable background conditions are illustrated in Fig. 2 by the low number of counts at low and high time channel numbers.

Figure 3 shows a scatter plot of neutron TOF versus light output of the scintillator induced by a neutron. The intensity distribution outlines the correlation between neutron flight times and proton recoil energies. This correlation is important for the data analysis, as it allows further discrimination between neutrons and γ rays. For example, all events outside the region of high intensity in Fig. 3 were rejected in the final analysis. A calibration measurement was made using a ^{252}Cf source placed in the target position, where the neutrons from spontaneous fission were detected in coincidence with fission fragments using the same experimental setup.

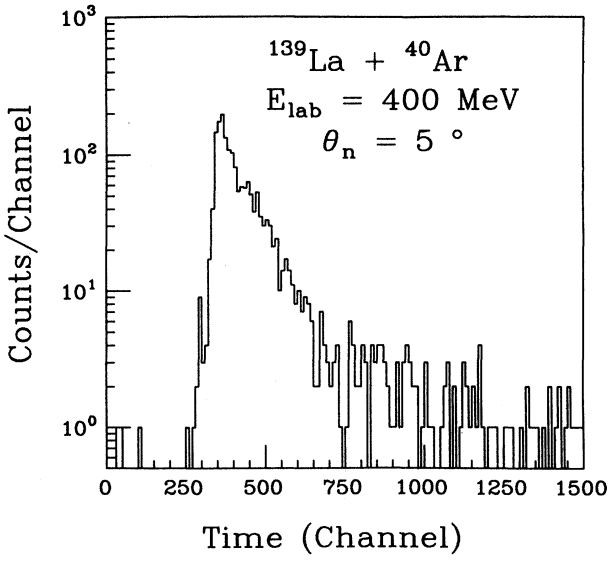

FIG. 2. Time-of-flight spectrum for all events identified as neutrons at a detection angle of $\theta_n = 5°$.

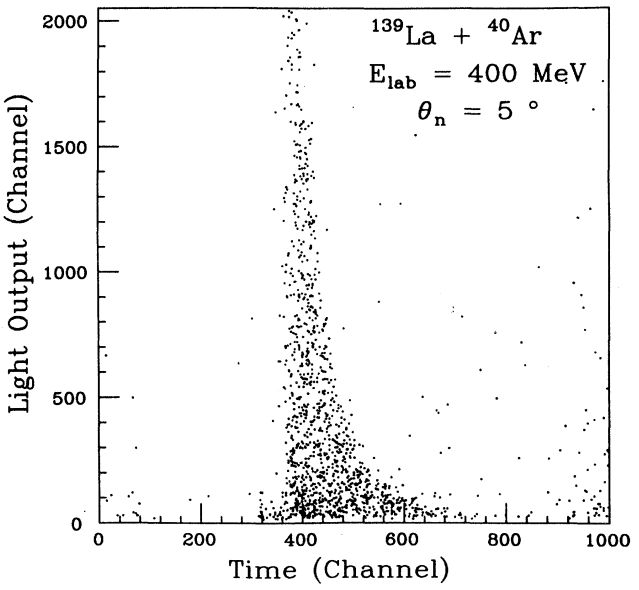

FIG. 3. Scatter plot of light output versus time of flight for events in Fig. 2. Events not correctly correlated were later eliminated.

III. DATA ANALYSIS AND RESULTS

The data analysis and calculations presented in this paper were performed on the VAX clusters of the University of Rochester Nuclear Structure Research Laboratory and Medical Center Computing facility, as well as on the Cornell Theory Center IBM 3090. The energies deposited by the reaction fragments in the solid-state transmission and stop detectors were converted on an event-by-event basis to PLF atomic number (Z) and laboratory kinetic energy. The results of this conversion are shown in the two-dimensional scatter plot in Fig. 4 where the atomic number Z is plotted versus the laboratory energy of the PLF. The elastic peak at a Z of 18 and an energy of 375 MeV is evident, as is the good Z resolution of the solid-state detector telescope. The figure indicates a strong drift of the PLF atomic number distribution towards lower Z values, as the PLF energy decreases (energy loss increases). This drift represents a superposition of the effects of nucleon exchange and sequential charged-particle evaporation, so caution must be exercised when interpreting this figure.

The energy loss or reaction Q value was calculated iteratively from the detection angle of $\theta_{HI} = -20°$, the charge, and the energy of the secondary PLF, assuming two-body kinematics. Using a mass-to-charge ratio of 2.22 (A/Z for ^{40}Ar), an approximate PLF velocity was calculated. In the first step of the iteration, particle evaporation was neglected, and approximate values of the velocity and mass of the TLF and the kinetic energy loss

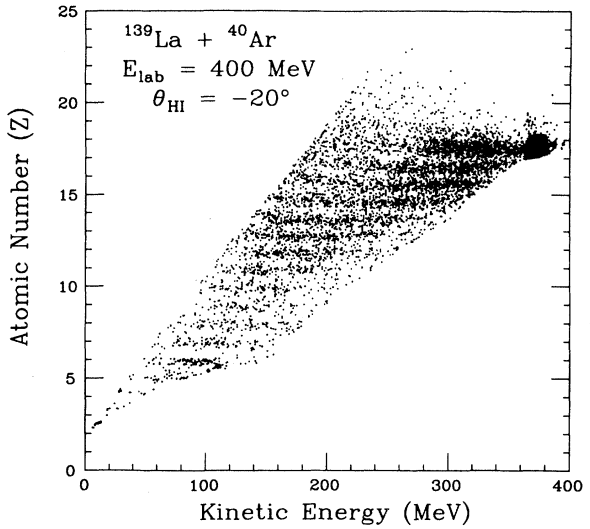

FIG. 4. Scatter plot of the post-evaporation atomic number (Z) vs kinetic energy for the PLF.

E_{loss} were obtained from momentum and mass conservation. Accounting for E_{loss} and Q_{gg} values for the reaction provided the first-order estimate for the total excitation energy, which was divided between the reaction fragments in proportion to their calculated masses. The number of neutrons evaporated from the PLF was then calculated to obtain an improved value for the PLF mass. With this new value for PLF mass, the calculation was repeated until the mass converged. In the final analysis, the experimentally determined excitation energy division was used to calculate the true energy loss.

The calculated velocity of the PLF was used to correct the measured neutron time of arrival for the time of flight of the PLF from the target to the solid-state detector. The resulting neutron TOF was converted on an event-by-event basis to energy scale, and the energy spectrum was then corrected for the efficiency of the neutron detector, which depends on neutron energy, scintillator geometry, and detector threshold.[19,20] This transformation was checked using both artificially generated neutron spectra and the data measured for neutrons emitted from spontaneous fission of ^{252}Cf which gave results that are in excellent agreement with the accepted values of Bowman *et al.*[21]

For each neutron event in a neutron detector at θ_n, the Jacobian factors $f_\nu(E_{lab},\theta_n,E_\nu,\theta_\nu,A_\nu)$ applying to the transformation from the laboratory to the emitter rest frame were calculated for both fragments. The quantities E_{lab}, θ_n, E_ν, θ_ν, and A_ν denote the measured neutron laboratory energy, the neutron detection angle, the emitting fragment laboratory energy, the neutron emission angle relative to the emitting fragment, and the emitting fragment mass, respectively (ν=PLF for projectile-like fragment, ν=TLF for target-like fragment). With these transformation factors, the double-differential multiplicity of neutrons $\overline{m}_\nu$ from emitter ν can be expressed as[2]

$$\frac{d^2\overline{m}_\nu}{d\Omega\, dE}=f_\nu C_\nu \frac{d^2\overline{m}}{(d\Omega\, dE)_{lab}} , \tag{1}$$

where $C_\nu(E_{lab},E_\nu,A_\nu)$ is the fraction of the total neutron multiplicity $\overline{m}$ that comes from the respective fragment. Assuming isotropic emission in the corresponding emitter rest frames, the double-differential multiplicity of neutrons in this frame can be written as[22]

$$\frac{d^2\overline{m}_\nu}{d\Omega\, dE}=\frac{\overline{m}_\nu}{4\pi}\frac{1}{\Gamma(n+1)}T_\nu^{-(n+1)}E^n\exp(-E/T_\nu) , \tag{2}$$

where T_ν is an effective nuclear temperature. If only one particle is evaporated, the shape of the spectrum is Maxwellian[23] (n=1), whereas for an evaporation cascade consisting of many neutrons it can be shown[22] that $n\simeq 0.45$ and $T_\nu\simeq\frac{11}{12}T_m$, where T_m is the nuclear temperature of the reaction fragment after the emission of its first neutron. It has been recently demonstrated[5] that this relationship between the quantity T_ν and the nuclear temperature cannot accurately be applied to reactions of this kind because the number of neutrons emitted by the individual fragments is not large enough. The measured quantity T_ν, therefore, has no simple connection to the temperature of the primary reaction fragment, and will henceforth be referred to as the logarithmic slope parameter of the neutron energy spectrum.

Converting the center-of-mass spectrum [Eq. (2)] to the laboratory frame, the energy distribution of neutrons emitted from a moving fragment is approximately given by[2]

$$\frac{d^2\overline{m}_\nu}{(d\Omega\, dE)_{lab}}=\frac{\overline{m}_\nu}{2}(\pi T)^{-3/2}E_{lab}^{1/2}\exp\{[E_{lab}-2(\epsilon_\nu E_{lab})^{1/2}\cos(\theta_\nu)+\epsilon_\nu]/T_\nu\} , \tag{3}$$

where E_{lab} is the neutron laboratory energy, θ_ν denotes the laboratory neutron emission angle measured from the direction of flight of the emitter, and ϵ_ν is the kinetic energy per nucleon of the emitting fragment. The contributions of the PLF and TLF to the total experimental neutron multiplicity were deduced in an event-by-event, iterative procedure, for each considered bin of energy loss. To obtain initial values of $\overline{m}_\nu$ and T_ν, two functions of the form given by Eq. (3) were fit to the experimental neutron distributions, using fixed, average values for the quantities ϵ_ν and θ_ν. The neutron intensity represented by each event was then divided between the PLF and TLF according to the fractions C_{PLF} and C_{TLF}, calculated with these quantities of $\overline{m}_\nu$ and T_ν and the experimental values of ϵ_ν and θ_ν for that event. The fractional intensities were then transformed into the rest frames of the respective emitters. Fits to the accumulated rest frame spectra performed with Eq. (2) provided improved values

for $\bar{m}_v$ and T_v. The procedure was repeated until these values had converged.

The above decomposition procedure accounts for the fluctuations in both emitter velocities and scattering angles. The results of this process are illustrated in Fig. 5, where the differential multiplicity of neutrons from the PLF (circles) and TLF (squares) is plotted versus energy in the respective emitter rest frames. The TLF spectra have been multiplied by a factor of 0.1 for better presentation. Circles are absent in four of the spectra, integrated over fragment Z values and energy losses greater than 20 MeV, due to the strong kinematical focusing of the PLF in the laboratory (see Fig. 8). The solid curves shown in Fig. 5 correspond to fits of Eqs. (2) with $n=0.45$ to the experimental spectra. It is evident from the figure that there is a high-energy spectral component in the energy distribution associated with the PLF in excess of the evaporation spectrum. This component is not the result of γ rays contaminating the neutron TOF spectrum, as the high-energy events have a correct correlation between light output and TOF (see Fig. 3). High-energy spectral components have been recognized as a signature[24] of preequilibrium neutron emission in other reactions of heavy-ions in this bombarding energy regime. Therefore, in order to identify this component in the spectra, the laboratory fits were redone, including a hypothetical third source [Eq. (3)] moving in the direction of the beam, whose velocity, multiplicity, and slope parameter were taken to be free fit parameters, increasing the total number of fit parameters to seven.

The laboratory energy distributions and the best three-source fits are shown in Fig. 6. The dashed curve in Fig. 6 represents the component of the fit coming from the PLF, the dotted curve represents the TLF contribution to the fit, and the dot-dashed curve represents the third component, whose velocity and spectral slope parameter (discussed later) are consistent with preequilibrium neutron emission. The solid curve is the sum of all three components. One can see that this fit describes the data very well at all angles. In recent literature,[25] it has been pointed out that the laboratory energy distributions of preequilibrium neutrons are most likely much more complicated than the simple parametrization presented in the fit. It must be emphasized here that this hypothetical third source is not necessarily a single physical emitter; it merely provides a tentative separation of the preequilibrium component from the evaporation spectra.

Figure 7, then, shows the energy spectra of neutrons from the projectile-like fragment (circles) and target-like fragment (squares) in their respective emitter rest frames deduced from an iterative transformation as discussed above, but assuming three emission sources. The solid curves shown in Fig. 7 correspond to fits of Eq. (2) with

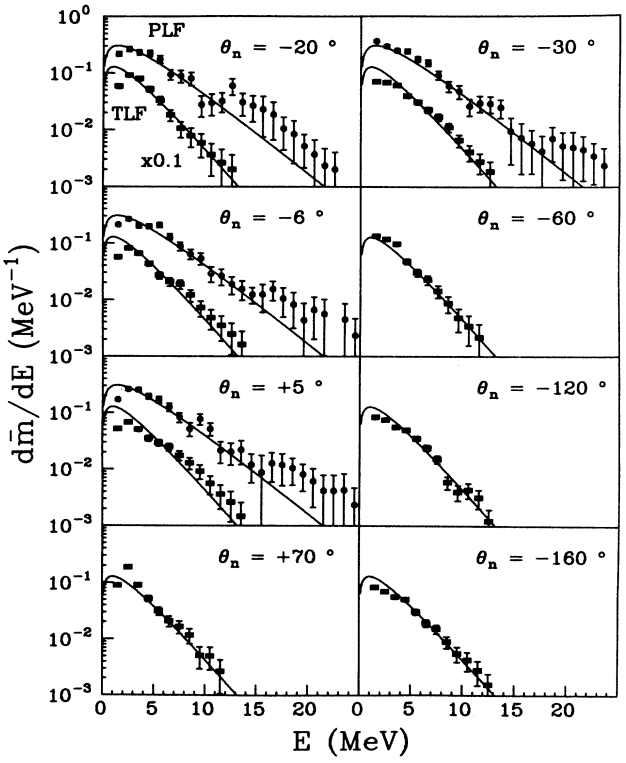

FIG. 5. Neutron energy distributions in the corresponding emitter rest frames, assuming only two emission sources. Squares are the data for neutrons from the target-like fragment and circles are the data for neutrons from the projectile-like fragment. The solid curves are fits of the data with Eq. (2).

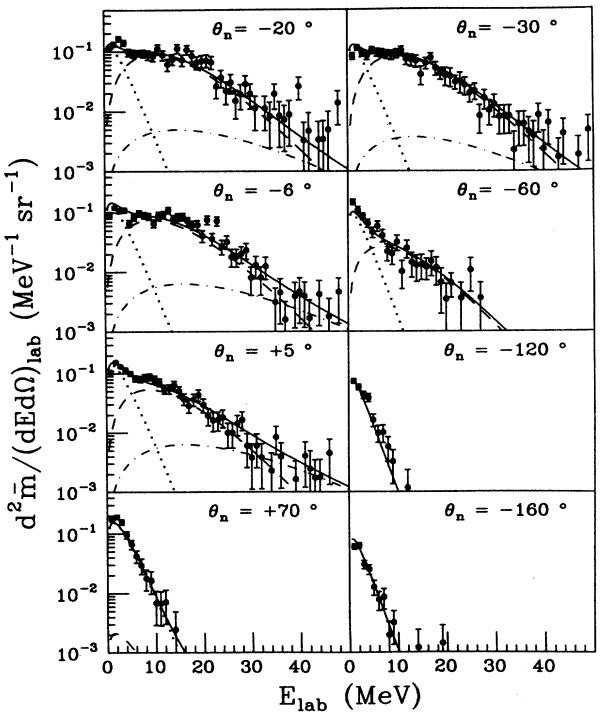

FIG. 6. Laboratory energy distributions for all neutron detectors. Circles are the data. The solid curve represents a three-source fit taking into account emission from target-like (dotted curve), projectile-like (dashed curve), and preequilibrium (dot-dashed curve) sources.

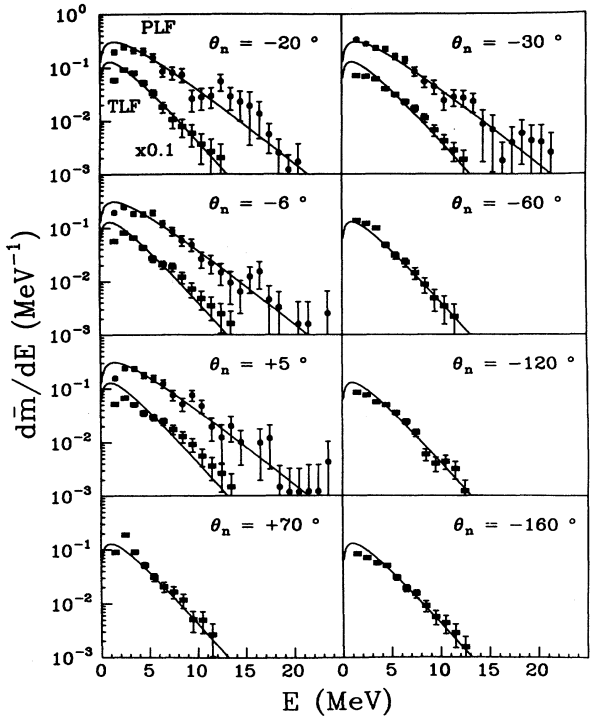

FIG. 7. Neutron energy distributions in the emitter rest frame, assuming three emission sources. Squares are the data for neutrons from the target-like fragment and circles represent the corresponding data for the projectile-like fragment. The solid curves are fits of the data with Eq. (2).

$n=0.45$ to the experimental spectra. Parameters deduced from fits performed independently for each angle were found to agree with each other within the experimental error. The slope parameters and multiplicities were then fixed to those found at forward angles for neutrons from the PLF, and those found at backward angles for neutrons from the TLF. The theoretical fits to the experimental neutron energy spectra illustrated in Figs. 5 and 6 correspond to a slope parameter of $T_{\rm PLF}=(2.24\mp0.20)$ MeV and a multiplicity of $\bar{m}_{\rm PLF}=(2.45\mp0.17)$ neutrons from the projectile-like fragment, and $T_{\rm TLF}=(1.61\mp0.12)$ MeV and $\bar{m}_{\rm TLF}=(3.70\mp0.20)$ neutrons from the target-like fragment. The slope parameter for the third, preequilibrium component was found to be $T_{\rm PRE}=(5.87\mp1.23)$ MeV with an apparent source whose flight path was in the direction of the beam and whose speed was (0.57 ∓ 0.12) times the velocity of the beam, and whose neutron multiplicity was $\bar{m}_{\rm PRE}=(0.11\mp0.03)$. The uncertainties in the measured values were calculated from statistical and systematic errors. The statistical error was determined by the quality of the fit, while the systematic errors were mainly due to the experimental time resolution, which corresponds to an error of 4.7% for 5 MeV neutrons and 16% for 50 MeV neutrons. The effect of the time resolution on the fits to the experimental neutron energy distributions was calculated from fits to synthetic spectra folded with the experimental resolution.

Integrating Eq. (3) over all energies, the approximate laboratory neutron angular distribution becomes[2]

$$\frac{d\bar{m}_\nu}{d\Omega}=\frac{\bar{m}_\nu}{2}\pi^{-3/2}\exp(a^2-\epsilon_\nu/T_\nu)\times\{\pi^{1/2}(a^2+0.5)[1-\mathrm{erf}(c)]+(2a+c)e^{-c^2}\}\ , \tag{4}$$

where $c=(E_s/T_\nu)^{1/2}-a$, $a=(\epsilon/T_\nu)^{1/2}\cos(\theta_\nu)$, and E_s the neutron detector energy threshold. Summing two components of the functional form given by Eq. (4), with slope parameters and multiplicities determined by the fits in Fig. 7, the data can be very well described as shown in Fig. 8, where the solid curve represents a sum of two components. In the laboratory frame neutrons emitted from the PLF (dashed curve) are strongly focused in the direction of flight of the PLF, while neutrons from the TLF (dotted curve) are emitted almost isotropically. The agreement of the data with the assumed two-source description suggests that the vast majority of neutrons come from sequential decay of the two fully accelerated reaction fragments.

Since the data at low and intermediate neutron energies are consistent with the picture of two sources emitting isotropically in their rest frames, it is justified to integrate the spectra for each fragment over the neutron angle, in order to gain the statistics needed to group data according to total kinetic energy loss. Figure 9 shows the integrated center-of-mass energy distributions of neutrons from the PLF and TLF and the fits to the data, for various values of total kinetic energy loss indicated in each panel. The circles represent distributions of neutrons from the projectile-like fragments, while the squares are the corresponding data for the target-like fragments. The neutron data in coincidence with the out-of-plane SSD were included in these angle-integrated spectra. The statistical quality of the data obtained with this telescope did not justify a separate, detailed analysis. Close examination of this figure shows that both the multiplicities and the slope parameters increase with increasing energy loss. One also observes that the slope parameters of the energy spectra of neutrons from the PLF and TLF are different from one another, for all values of energy loss. As has been pointed out previously,[5] this is not necessarily an indication that the dinuclear system has not achieved thermal equilibrium, because for these reactions, there is no trivial relationship between the slope of the neutron energy spectrum and the temperature of the emitting nucleus.[5]

IV. DISCUSSION

A. Energy relaxation

Since previous experiments[1] have demonstrated considerable success for the nucleon exchange model (NEM) in describing the first and second moments of the charge and mass distributions in damped heavy-ion collisions, it

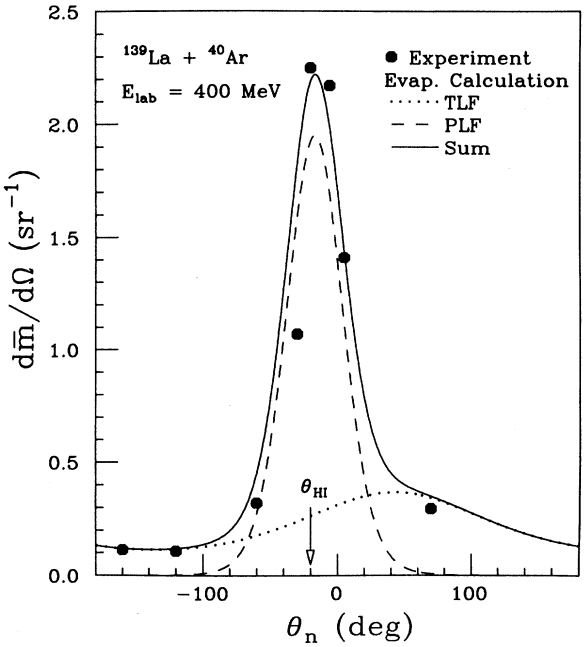

FIG. 8. Neutron angular distribution. Circles are the data, while the solid curve is an evaporation calculation taking into account emission from the target-like (dotted curve) and projectile-like (dashed curve) fragments. The statistical errors are smaller than the data points. The arrow indicates the detection angle θ_{HI} of the PLF.

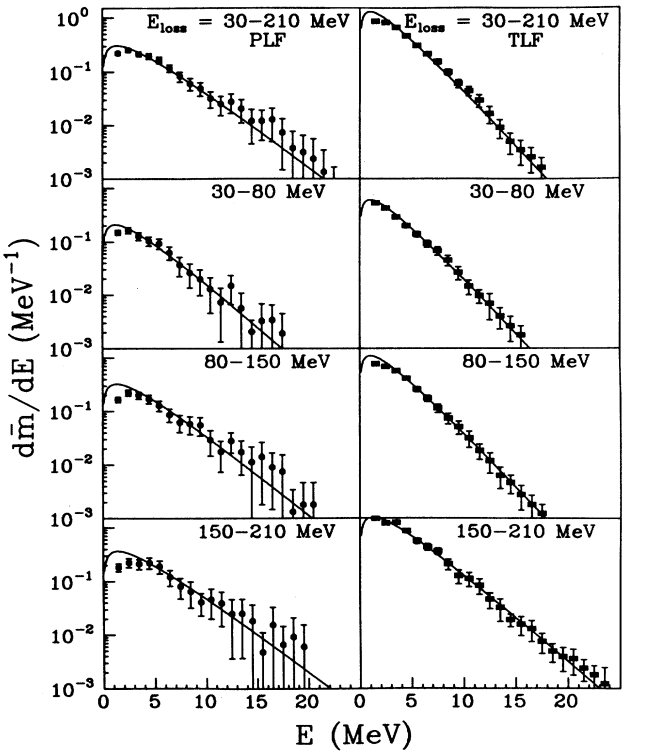

FIG. 9. Neutron energy distributions for a number of total kinetic-energy loss bins. The circles represent the neutrons from the projectile-like fragment, while the squares represent the data for the target-like fragment. The solid curves are fits of the data with Eq. (2).

is interesting to investigate the predictions of the NEM for the ^{139}La+^{40}Ar reaction at E_{lab}=400 MeV. In order to illustrate the predictions of the NEM for this reaction, Fig. 10 shows the NEM description of the behavior of the dinuclear system during its interaction phase in terms of four physical quantities: the area of the neck opening $\pi\rho^2$ [Fig. 10(a)], the variance σ_n^2 of the neutron number distribution [Fig. 10(b)], the ratio of the PLF velocity v_{PLF} over the beam velocity v_{beam} [Fig. 10(c)], and the temperatures τ_{PLF} and τ_{TLF} of the projectile-like (solid curve) and target-like (dashed curve) reaction fragments [Fig. 10(d)], respectively, as a function of collision time for a representative angular momentum of $l=135\hbar$. It can be seen from Fig. 10 that as the two nuclei initially come together, the neck begins to open [Fig. 10(a)]; energy is dissipated quickly [Fig. 10(c)]; the number of neutrons exchanged (represented by σ_n^2) increases steadily [Fig. 10(b)]; and a large thermal disparity between the two fragments develops [Fig. 10(d)]. As the neck reaches its largest opening, close to the classical turning point (indicated in the figure by an arrow), the amount of kinetic energy dissipated [Fig. 10(c)] begins to level off, as most of the available energy has already been damped. On the same time scale, the number of neutrons exchanged [Fig. 10(b)] rises steadily until it finally saturates when the neck breaks. The thermal disparity $\Delta\tau=\tau_{PLF}-\tau_{TLF}$ [Fig. 10(d)] between the two fragments decreases, although the system remains far from equilibrium even after the two nuclei have ceased to interact. As will be seen later, this predicted thermal disparity is in good agreement with the data. It is also interesting to note that the rate of exchange of neutrons [Fig. 10(b)] in this reaction remains rather constant throughout the interaction time. It is reasonable to assume, in the confines of this model, that any preequilibrium emission that takes place during the interaction of the dinucleus should be correlated with the number of neutrons transferred. If this is the case, the average "source velocity" of the preequilibrium component should be roughly equal to the velocity of the PLF halfway through the interaction phase, which, from Fig. 10(c) is approximately 0.70 times the velocity of the beam. This number is consistent with the experimental source velocity reported above.

Figure 11 shows the degree to which the NEM can predict the first and second moments of the PLF charge distribution. In this figure, the first moment [Fig. 11(a)] and the second moment [Fig. 11(b)] of the PLF element distribution are plotted as a function of energy loss for a detection angle of $\theta_{HI}=-20°$. Although these data are measured at only one angle, they are representative of the overall distribution, since the energy-differential element distributions are not expected to change very much with angle.[1] The data show that with increasing energy loss,

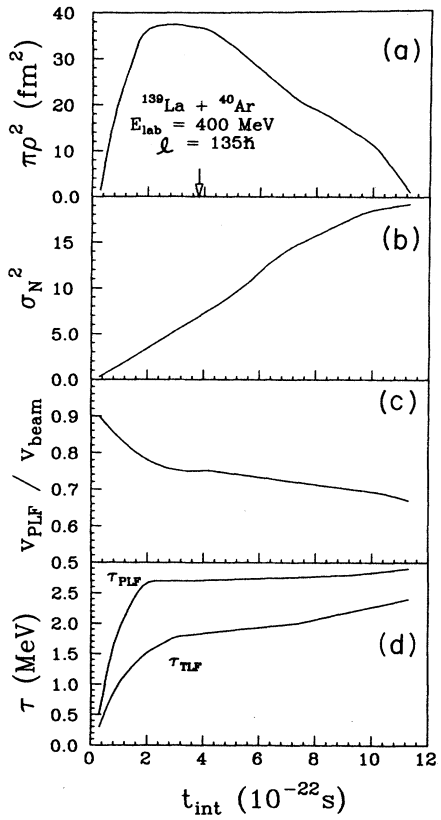

FIG. 10. Predictions by the nucleon exchange model of the time evolution of the area of the neck opening, $\pi\rho^2$ (a); the variance of the neutron number distribution, σ_n^2 (b); the ratio of the PLF velocity, v_{PLF}, over the velocity of the beam, v_{beam} (c); and the temperatures of the two fragments (d). The arrow represents the classical turning point in the PLF trajectory.

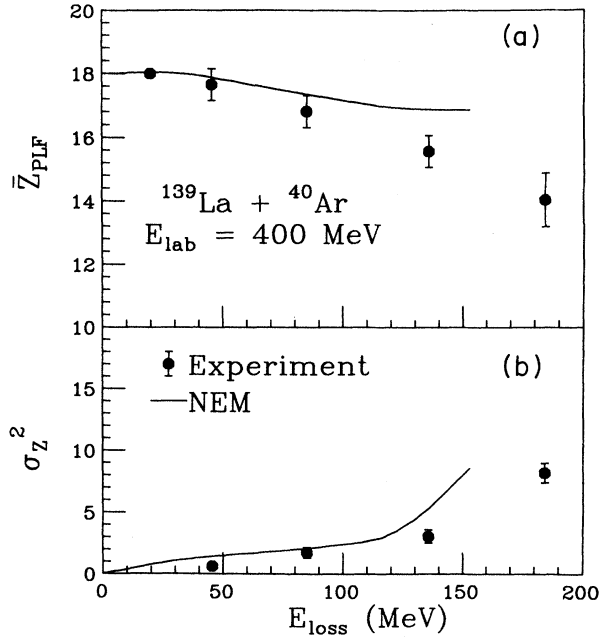

FIG. 11. The first (a) and second (b) moments of the PLF atomic number distribution versus energy loss. The circles are the data, while the solid curves are the NEM predictions corrected for sequential evaporation.

the PLF loses charge on the average, and the width or variance σ_Z^2 of its element distribution increases. The solid curves represent the predictions of the NEM, which are corrected for evaporation in a detailed application of the statistical model code PACE (Ref. 26) described below. Although the NEM underestimates the magnitude of the drift of the element distribution at large energy losses, the overall trends of the data are reproduced quite well. Hence, it is interesting to compare the theoretically predicted evolution of the thermal disparity with energy loss to the experimental data.

The ratio T_{TLF}/T_{PLF} of the slope parameters characterizing the experimental energy spectra for the neutrons from the TLF to that for neutrons from the PLF is plotted in Fig. 12(a) versus total kinetic energy loss E_{loss}. One can see from this plot that the experimental slope parameters for the correlated fragments become nearly equal to each other, within statistical error, only for the highest total kinetic-energy loss bin. Since the correspondence between energy loss and interaction time is well documented in the literature, it follows that for short interaction times ($E_{loss} \sim 60$ MeV) the disparity between the

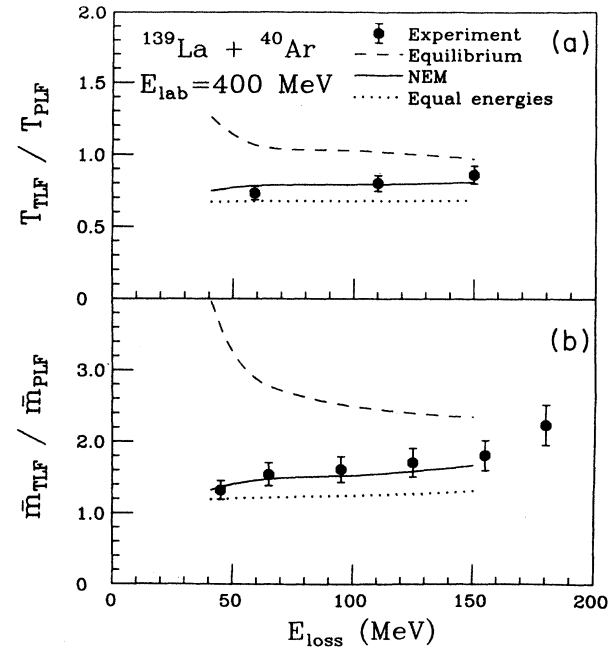

FIG. 12. The ratio of the slope parameters (a) and the ratio of the multiplicities (b) characterizing the energy spectra of neutrons from the target-like and projectile-like fragments. The circles are the data, and the three curves are based on different excitation energy divisions as described in the text.

slope parameters is quite significant, but decreases for increasing interaction time.

The curves in Fig. 12(a) correspond to results of detailed statistical calculations employing the computer code PACE. The calculations were performed in the following manner. For each energy loss bin, primary projectile-like and target-like fragment distributions were calculated using the one-body nucleon exchange model (NEM). Then, sequential decay of these excited primary fragments was simulated in a PACE calculation performed for each fragment in this distribution with a relative probability of greater than 1 percent. Two sets of assumptions must be made at this point in the calculation. First, the values for the parameters governing the statistical decay of the nuclei are adopted. Except for the level density parameter a (discussed below), all values for these statistical parameters are taken from systematics.[26] The second assumption refers to the partition of available excitation energy between the reaction fragments. Three different choices, covering the range of possibilities, were made for this assumption: thermal equilibrium (dashed curve), equal energy division (dotted curve), and the division given by the NEM (solid curve). Additionally, in damped nuclear reactions, for a fixed energy loss, the distribution of excitation energies generated in each fragment has a finite width. In these calculations, the excitation energy distribution for each fragment was assumed to be Gaussian, with a width given by equilibrium conditions.[27] For each fragment and energy loss bin, five PACE calculations were performed using different points along the assumed excitation energy distribution (one at the maximum, two at half maximum, and two at 15% of the maximum). The PACE calculations were performed neglecting the relatively small effect of fragment spin[5] and with a level density parameter of $a_{\mathrm{PLF}}=A_{\mathrm{PLF}}/8.0$ MeV^{-1} for the PLF and $a_{\mathrm{TLF}}=A_{\mathrm{TLF}}/12.0$ MeV^{-1} for the TLF. The motivation for using these values of a will be discussed below. The resulting neutron energy distributions and multiplicities were then integrated according to the theoretical abundance of the primary reaction fragment and the relative probability on the excitation energy distribution, and the final neutron energy spectra were fitted with Eq. (2) ($n=0.45$). The result of such a long and complicated calculation is a detailed statistical prediction of the neutron energy distributions and multiplicities for a damped heavy-ion reaction, for each assumed excitation energy division.

It can be seen from the figure that the data are consistent with the projectile-like fragment receiving close to 50% of the total excitation energy at 60 MeV of energy loss, with a gradual approach to equilibrium as energy loss increases. The NEM prediction (solid curve), agrees quite well with the data, suggesting that the microscopic physical processes included in the model are largely responsible for the macroscopic energy relaxation mechanism observed in the experiment.

Figure 12(b) is a plot of the ratio of the multiplicity of neutrons from the TLF over the multiplicity of neutrons from the PLF. The curves represent the calculations discussed above. It turns out[5] that the calculated multiplicity ratios are relatively insensitive to the assumed statistical parameters such as the level density parameter a because the changes in the energy of the emitted neutrons induced by varying these parameters are small compared to the neutron binding energy. The ratio of the slope parameters, however, depends on a as the level density parameter strongly influences the nuclear temperature. Thus, a number of the above calculations were performed, varying the level density parameter a. In each case, the ratios of the multiplicities are well described by the NEM, but only in the case where $a_{\mathrm{PLF}}=A_{\mathrm{PLF}}/8.0$ MeV^{-1} and $a_{\mathrm{TLF}}=A_{\mathrm{TLF}}/12.0$ MeV^{-1} did the NEM prediction fit both the multiplicity and slope parameter ratios. Since these two sets of data must be in agreement, the values for the level density parameters used above are considered reasonable assumptions. Previous fusion experiments[28,29] indicate that near the $N=82$ neutron shell, $a=A/12.0$ is the most reasonable choice for the level density parameter, in agreement with the present calculations. The multiplicity data are in good agreement with the slope parameter data, suggesting that at very low energy losses the projectile-like fragment gets nearly 50% of the total excitation energy. For larger energy losses, the system approaches thermal equilibrium, in agreement with the predictions of the NEM. The NEM predictions not only agree with the multiplicity and slope parameter ratios but also agree with the absolute values for the multiplicity and slope parameter for neutrons from each reaction fragment.

B. Preequilibrium neutron emission

The source fits to the laboratory energy distributions illustrated in Fig. 5 contain a small but statistically significant contribution from a high-energy "preequilibrium" component. Summed over all values of E_{loss}, the multiplicity of neutrons from this component is (0.11 ∓ 0.03); however, as shown in Fig. 13, these data depend on E_{loss}. Here, the multiplicity of this "preequilibrium" component is plotted as a function of energy loss. Although the error bars, which include both systematic and statistical uncertainties, overlap somewhat, the trend is quite clear: a higher preequilibrium neutron multiplicity for higher energy loss. This dependence has been seen in other data,[30] and it can be understood in the framework of the Fermi-jet model.[31]

In this model, when a nucleon is transferred from one nucleus to another, the coupling of its Fermi velocity and the relative velocity of the two nuclei can boost the nucleon sufficiently to allow it to escape the dinucleus. This effect is more important for low values of impact parameter (high energy loss), as the velocities of the nucleons being transferred are more aligned with the relative velocity in central collisions. In addition, more neutrons are transferred as the impact parameter decreases, so the number of escapes should increase accordingly. This energy-loss dependence of the preequilibrium neutron multiplicity is illustrated by the calculations presented in Fig. 13 which are results obtained with a Fermi-jet code.[32] The solid curve is the prediction of this code for the total number of preequilibrium neutrons as a function of energy loss. As one can see, this calculation over-

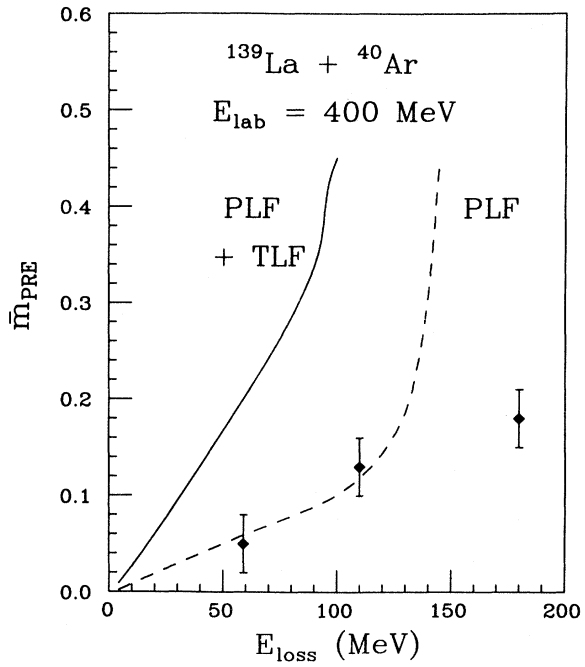

FIG. 13. The multiplicity of the preequilibrium neutrons as a function of energy loss. The diamonds are the data, while the solid curve is the prediction of the Fermi-jet model including neutrons from both fragments. The dashed curve includes neutrons from the PLF only.

predicts the data. However, it has been pointed out[32] that the calculation predicts two components of preequilibrium neutrons: one forward focused component corresponding to Fermi jets that originate in the PLF, and one backward focused component corresponding to Fermi jets that originate in the TLF. The preequilibrium multiplicity was extracted from the data in this experiment assuming only a forward-peaked component. The Fermi jets from the TLF are predicted to have low laboratory kinetic energies and could possibly be masked by the evaporated neutrons. Therefore, perhaps it is more correct to compare the data to the dashed curve, which is the prediction for Fermi jets originating only in the PLF. The magnitude of the data is now well reproduced at low and intermediate energy losses; however, the dependence of the calculated preequilibrium neutron multiplicity on energy loss is much stronger than the data indicate for high energy losses.

Although the predicted preequilibrium neutron multiplicity is in good agreement with the data at the lower energy losses, care must be taken in drawing concrete conclusions from Fig. 13. The poor statistical quality of the preequilibrium neutron data, coupled with the low preequilibrium neutron multiplicity, allows only qualitative comparisons of the neutron energy spectra with the Fermi-jet calculation. The predicted Fermi-jet energy spectra have a larger fraction of low-energy neutrons than the parametrization employed to extract the preequilibrium component, and the predicted Fermi-jet angular distribution is also significantly different from the parametrization employed. An experiment conducted at a higher bombarding energy would be very useful for a rigorous comparison to the Fermi-jet model, as the higher bombarding energy would enhance[1] the preequilibrium neutron multiplicity.

V. CONCLUSIONS

The presently reported exclusive data on energy and angular distributions of neutrons emitted in damped ^{139}La+^{40}Ar collisions at E_{lab}=400 MeV have shown that the dominant sources of neutrons are the fully accelerated light and heavy reaction fragments. Two quasi-independent aspects of the data, the spectral shapes and the associated neutron multiplicities, have been analyzed, and they both were found to consistently reveal clear signatures of a thermal disparity between the two reaction partners. The thermal disparity is especially large at the initial stage of the collision, identified experimentally with low-E_{loss} events. As the system progresses towards large kinetic energy damping, i.e., long-interaction times, the thermal disparity decreases, and the system approaches equilibrium. It has been shown in this work that the above trends can be described quantitatively by the one-body nucleon exchange transport model. In addition, detailed analysis of the neutron energy distributions has revealed the presence of a small component originating from a source different from either of the two fully accelerated reaction fragments. This component exhibits a large spectral slope parameter and correlations that can be simulated by a hypothetical source moving with half the beam velocity, and has therefore been attributed to preequilibrium neutron emission. Although its energy loss-averaged multiplicity is rather low ($\bar{m}_{PRE}$=0.11 $\mp$0.03), this component shows a clear and definite dependence on kinetic-energy loss and thus the impact parameter. There are very few preequilibrium neutrons emitted in small-E_{loss} events associated with large impact parameters; however, with increasing energy loss (decreasing impact parameters) the probability for preequilibrium emission increases substantially. The rate of this increase, however, could not be reproduced quantitatively in theoretical calculations based on the Fermi-jet model. Observations of such new trends in preequilibrium neutron emission in damped nuclear reactions warrants performing specially optimized experiments on the same system at elevated bombarding energies.

ACKNOWLEDGMENTS

We gratefully acknowledge the kind hospitality extended to us during our experiment at the Lawrence Berkeley Laboratory 88-inch Cyclotron facility. In particular, we deeply appreciate the help and support by Yuen-dat Chan in getting us started at this facility. We also gratefully acknowledge the use of the Fermi-jet code by J. Randrup and R. Vandenbosch. This work was supported by the U.S. Department of Energy under Grant No. DE-FG02-88ER40414.

*Present address: Michigan State University, National Superconducting Cyclotron Laboratory, East Lansing, MI 48824-1321.

[1]W. U. Schröder and J. R. Huizenga, in *Treatise on Heavy-Ion Science,* edited by D. A. Bromley (Plenum, New York, 1984), Vol. 2, and references cited therein.

[2]D. Hilscher, J. R. Birkelund, A. D. Hoover, W. U. Schröder, W. W. Wilcke, J. R. Huizenga, A. C. Mignerey, K. L. Wolf, H. F. Breuer, and V. E. Viola, Jr., Phys. Rev. C **20**, 576 (1979).

[3]B. Tamain, R. Chechik, H. Fuchs, F. Hanappe, M. Morjean, M. Dakowski, B. Lucas, C. Mazur, M. Ribrag, and C. Signarbieux, Nucl. Phys. **A330**, 253 (1979).

[4]I. Tserruya, A. Breskin, R. Chechik, Z. Fraenkel, S. Wald, N. Zwang, R. Bock, M. Dakowski, A. Gobbi, H. Sann, R. Bass, G. Kreyling, R. Renfordt, K. Stelzer, and U. Arlt, Phys. Rev. C **26**, 2509 (1982).

[5]J. L. Wile, W. U. Schröder, J. R. Huizenga, and D. Hilscher, Phys. Rev. C **35**, 1608 (1987).

[6]J. R. Huizenga, W. U. Schröder, J. R. Birkelund, and W. W. Wilcke, Nucl. Phys. **A387**, 257c (1982).

[7]T. C. Awes, R. L. Ferguson, R. Novotny, F. E. Obenshain, F. Plasil, S. Pontoppidan, V. Rauch, G. R. Young, and H. Sann, Phys. Rev. Lett. **52**, 251 (1984).

[8]R. Vandenbosch, A. Lazzarini, D. Leach, D. K. Lock, A. Ray, and A. Seamster, Phys. Rev. Lett. **52**, 1964 (1984).

[9]H. Sohlbach, H. Freiesleben, P. Braun-Munzinger, W. F. W. Schneider, D. Schüll, B. Kohlmeyer, M. Marinescu, and F. Pühlhofer, Phys. Lett. **153B**, 386 (1985); Nucl. Phys. **A467**, 349 (1987).

[10]S. B. Gazes, H. R. Schmidt, Y. Chan, E. Chavez, R. Kamermans, and R. G. Stokstad, Phys. Rev. C **38**, 712 (1988).

[11]H. R. Schmidt, S. B. Gazes, Y. Chan, R. Kamermans, and R. G. Stockstad, Phys. Lett. B **180**, 9 (1986).

[12]K. Siwek-Wilczynska, R. A. Blue, L. H. Harwood, R. M. Ronningen, H. Utsunomiya, J. Wilczynski, and D. J. Morrissey, Phys. Rev. C **32**, 1450 (1985).

[13]L. G. Sobotka, G. J. Wozniak, R. J. McDonald, M. A. McMahan, R. J. Charity, L. G. Moretto, Z. H. Liu, F. S. Stephens, R. M. Diamond, M. A. Deleplanque, and A. J. Pacheco, Phys. Lett. B **175**, 27 (1986).

[14]D. R. Benton, H. Breuer, F. Khazaie, K. Kwiatkowski, V. E. Viola, S. Bradley, A. C. Mignerey, A. P. Weston-Dawkes, and R. J. McDonald, Phys. Lett. B **185**, 326 (1987).

[15]H. Keller, R. Bellwied, K. Lützenkirchen, J. V. Kratz, W. Brüchle, H. Gäggler, K. J. Moody, M. Schädel, and G. Wirth, Z. Phys. A **328**, 255 (1987).

[16]H. Gäggler, W. Brüchle, M. Brügger, M. Schädel, K. Sümmerer, G. Wirth, J. V. Kratz, M. Lerch, Th. Blaich, G. Herrmann, N. Hildebrand, N. Trautmann, D. Lee, K. J. Moody, K. E. Gregorich, R. B. Welch, G. T. Seaborg, D. C. Hoffman, W. R. Daniels, M. M. Fowler, and H. R. von Gunten, Phys. Rev. C **33**, 1983 (1986).

[17]J. Randrup, Nucl. Phys. **A307**, 319 (1978); **A327**, 490 (1979).

[18]T. Døssing and J. Randrup, Nucl. Phys. **A433**, 215 (1985); **A433**, 280 (1985).

[19]A. Del Guerra, Nucl. Instrum. Methods **135**, 337 (1976).

[20]R. A. Cecil, B. D. Anderson, and R. Madey, Nucl. Instrum. Methods **161**, 439 (1979).

[21]H. R. Bowman, S. G. Thompson, J. C. D. Milton, and W. J. Swiatecki, Phys. Rev. **126**, 2120 (1962).

[22]K. J. Lecouteur and D. W. Lang, Nucl. Phys. **13**, 32 (1959); **53**, 113 (1964).

[23]V. Weisskopf, Phys. Rev. **52**, 295 (1937).

[24]M. Blann, Phys. Rev. C **23**, 245 (1981); **31**, 1245 (1985).

[25]M. Blann and B. Remington, Phys. Rev. C **37**, 2231 (1988).

[26]A. Gavron, Phys. Rev. C **21**, 230 (1980).

[27]D. J. Morissey and L. G. Moretto, Phys. Rev. C **23**, 1835 (1981).

[28]W. Kühn, P. Chowdhury, R. V. F. Janssens, T. L. Khoo, F. Haas, J. Kasagi, and R. M. Ronningen, Phys. Rev. Lett. **51**, 1858 (1983).

[29]J. L. Wile, S. S. Datta, W. U. Schröder, J. Toke, R. T. de Souza, and J. R. Huizenga, U.S. Department of Energy Progress Report C00-3496-82, 1987, J. R. Huizenga and W. U. Schröder, principal investigators, pp. 443–457.

[30]A. Kiss, F. Deak, Z. Seres, G. Caskey, A. Galonsky, L. Heilbronn, and B. Remington, Phys. Rev. C **38**, 170 (1988).

[31]J. P. Bondorf, J. N. De, G. Fai, A. O. T. Karvinen, B. Jakobsson, and J. Randrup, Nucl. Phys. **A333**, 285 (1980).

[32]J. Randrup and R. Vandenbosch, Nucl. Phys. **A474**, 219 (1987).